Self-sustained snapping drives autonomous dancing and motion in free-standing wavy rings

Yao Zhao, Yaoye Hong, Fangjie Qi, Yinding Chi, Hao Su, Jie Yin*

Y. Zhao, Y. Hong, F. Qi, Y. Chi, H. Su, J. Yin

Department of Mechanical and Aerospace Engineering, North Carolina State University, Raleigh, NC 27695, USA

*E-mail: jyin8@ncsu.edu

Abstract: Harnessing snapping, an instability phenomenon observed in nature (e.g., Venus flytraps), for autonomy has attracted growing interest in autonomous soft robots. However, achieving self-sustained snapping and snapping-driven autonomous motions in soft robots remains largely unexplored. Here, we report harnessing bistable, ribbon ring-like structures for realizing self-sustained snapping in a library of soft liquid crystal elastomer wavy rings under constant thermal and photothermal actuation. The self-sustained snapping induces continuous ring flipping that drives autonomous dancing or crawling motions on the ground and under water. The three-dimensional, free-standing wavy rings employ either a highly symmetric or symmetry-broken twisted shape with tunable geometric asymmetries. We find that the former favors periodic self-dancing motion in place due to isotropic friction, while the latter shows a directional crawling motion along the predefined axis of symmetry during fabrication due to asymmetric friction. It shows that the crawling speed can be tuned by the geometric asymmetries with a peak speed achieved at the highest geometric asymmetry. Lastly, we show that the autonomous crawling ring can also adapt its body shape to pass through a confined space that is over 30% narrower than its body size.

1. Introduction

This article has been accepted for publication and undergone full peer review but has not been through the copyediting, typesetting, pagination and proofreading process, which may lead to differences between this version and the Version of Record. Please cite this article as doi: 10.1002/adma.202207372.

Snapping, a fast shape-change motion induced by elastic instabilities, is often observed in nature and our daily life, e.g., snapping in Venus flytraps for fast closure and snapping in hemisphere shells for jumping toys. These structures are bistable and often possess two stable states in reverted curved shapes.[1] The two stable states can be reversibly switched via snapping to bypass the intermediate unstable state.[2-3] Snapping can be triggered by mechanical forces or various external stimuli, such as light,[4-6] heat,[4-5, 7] or magnetic field.[8-9] During snapping, the stored elastic strain energy can be quickly released, leading to a large output force and fast shape change motion.[10-12] Recently, harnessing the benefits of snapping in bistable and multistable structures made of various soft active materials has found broad applications in shape-morphing devices, soft actuators, and soft robotics.[1, 13-14] Snapping has enabled diverse unique functionalities, including amplified force and fast response,[15] high-speed motion (crawling,[16] swimming,[16-17] and jumping[18-21]), physical intelligence,[22] and mechanical memory operation.[23]

Among different soft active materials, anisotropic smart materials such as liquid crystal polymers (LCPs)[24-26] has recently attracted growing interest in untethered actuation and motion[27-30] due to their two-way shape memory effects. LCPs can reversibly shrink or elongate by shifting between the nematic and the isotropic states in response to thermal, photo, or chemical stimulations.[31-32] Light or heat-induced snapping is reported in various LCPs-based bistable soft active structures such as doubly clamped buckled strips,[6, 33-35] cylindrical shells,[36] twisted ribbons,[22] and circular bilayered rings.[37] However, snapping in most studies (not limited to LCPs) is not self-sustained without either manually changing the mechanical or stimuli-responsive actuation inputs[6, 16-21, 33] or imposing external physical constraints.[22, 34-35] This largely hinders their potential applications for untethered and autonomous motion in soft robots. Achieving self-sustained snapping under constant external stimuli remains challenging and yet largely unexplored, because it needs to repeatedly store and release the strain energy for autonomous reversible switch between two stable states in response to constant external stimuli.

Here, we report leveraging wavy ring geometry for achieving self-sustained snapping and autonomous motion in a library of freestanding liquid crystal elastomers (LCEs) rings in response to constant heat or light. In contrast to doubly clamped buckled strips,[6, 33-35] a circular elastic ring can undergo snapping instabilities under simple mechanical forces such as bending or twisting without the need of external physical constraints,[38-39] since the closed-loop ring shape imposes an intrinsic geometric constraint. We show that the snapping behavior and snapping-induced motion can be programmed by the geometric asymmetries during fabrication for autonomous periodic dancing or crawling motions on a hot surface or under infrared light. The highly symmetric LCE wavy ring can achieve steady-state, periodic dancing-like motions via snapping-induced non-stopping flipping. To achieve directional motion, we explore the strategy of introducing geometric asymmetries to break the symmetric shape changes in the wavy rings for asymmetric friction. Finally, we demonstrate its potential application as an adaptive autonomous soft crawler for passing through confined spaces.

2. Results and Discussion

2.1 Self-sustained snapping for autonomous dancing rings

The LCE wavy rings are fabricated by following the two-stage polymerization method[40-41] under radial mechanical stretching (see Materials and methods for more details). **Figure 1a** shows a representative first-stage cured LCE wavy ring (radius R_o = 10 mm, square cross section with thickness t_o = 2 mm) composed of continuous semicircles (20 semicircles with radius $r_o = R_o \tan(9^o)$ = 1.6 mm) through soft molding. The sample is then radially stretched and kept hooping around a rigid cylinder (diameter 5 cm) during the second-stage UV curing, as shown in **Figure 1b**. The mesogens can be aligned along the hoop direction by the circumferential stretching (**Figure S1**). After UV curing with stretching, the waves in the original planar ring start writhing out of plane to form a free-standing wavy ring (**Figure S2**) to reduce the elastic strain energy.

When placing on a hot surface with its surface temperature T_{surf} (e.g., T_{surf} = 120 °C) much higher than the nematic-isotropic transition temperature (T_{NI}) of the as-synthesized LCE (T_{NI} ≈ 80 °C), the wavy ring undergoes self-sustained continuous snapping, which drives periodic flipping of the ring (**Figures 1c-1f**). The bistable ring can autonomously and repeatedly flip inside out by snapping between the two stable states, i.e., the original (**Figures 1c, 1f (i)**) and flipped shape (**Figures 1e, 1f (v)**) with local minimum strain energy U_{min}, and bypassing the unstable state, i.e., the flattened ring shape (**Figures 1d, 1f (iii)**) with local maximum strain energy U_{max} (**Figure S3a**). The heterogeneous heating in the free-standing wavy ring provides the moment to drive the flipping by overcoming the energy barrier $\Delta U = U_{max} - U_{min}$ (**Figure S3a**).

Specially, upon discrete thermal contacts with the hot surface, the wave troughs on the bottom start to shrink toward the ring center due to the heat-induced shrinkage nature of LCEs (**Figures 2a-2c, Movie S1 and S2**), whereas the wave crests on the top shrink less due to the temperature gradient across the height (e.g., a temperature gradient from ~ 120 °C to ~ 90 °C as shown in **Figures 2c-2d**). Thus, the ring first deforms into a trumpet-like shape (**Figures 1f (ii), 2b**). Consequently, the originally balanced gravity and supporting forces at the contact points become misaligned (**Figures 1c**-**1d**), which generates moments that drive the outside flipping and blooming of the ring. After the flipping angle (**Figure S3b**) goes beyond a critical value of ~ 45° (**Figure 2e**), it quickly snaps through to a flipped trumpet-like shape within 112 ms (**Figure 1f (ii)**-**(iv)**), where the flipping angle increases dramatically to ~ 135° (**Figure 2e**), by bypassing the unstable flattened state (**Figure 1f (iii)**). After flipping, the waves on the bottom and the top are switched and become cooled down and heated up, respectively, driving further standing up of the ring (**Figure 1f (v)** and **Figure 2e**). By repeating the similar blooming- snapping process, the flipped ring can return to its original shape and dance periodically with the alternating cooling and heating of the top and bottom waves.

We note that unlike the self-sustained snapping induced steady-state, continuous flipping in the free-standing wavy ring, only transient flipping is observed in its counterpart circular ring without waves due to the non-self-sustained snapping (T_{surf} = 120 °C, **Figures S4a-4b**). After two trials of snapping, it shrinks to a smaller circular ring with its radius reduced by over 23% and becomes still. This is because in contrast to the discrete thermal contact and much higher height (~ 2.6 times) in the free-standing wavy ring, the shallow circular ring shows continuous contact that induces a lower temperature gradient ΔT across the height. Consequent flipping further lowers ΔT. Thus, after few trials of snapping, ΔT ~ 0 and the shallow ring becomes homogeneously heated with a shrunk size. We observe that further increasing the height of the circular ring results in a deformed trumpet-like shape without snapping and flipping (**Figures S4d-4e**) due to its much higher energy barrier induced by the geometric asymmetry of its cross section. It should be noted that when the ring takes a highly symmetric cross section, e.g., a torus shape with a circular cross section, it transits to a zero-energy mode for easily and continuously rolling inside-out or outside-in without snapping.[42]

Similar self-dancing wavy ring can also be achieved under remote photothermal actuation. When placing the ring under infrared (IR) light (e.g., an IR emitter), it snaps to flip outside in, in the opposite way to the thermal contact actuation, due to the larger shrinkage on the top (**Figure 1g, Figure S5, and Movie S3**). We note that the light-actuated ring exhibits more complicated out-of-plane bending deformation and circular-to-elliptical ring shape changes (**Figure 1g**), due to its more complex and heterogeneous spatial heating through IR light. Most of the areas exposed to IR have similar temperature and the temperature gradient is induced through contacting with the ground and self-shading (**Figure S6**). Meanwhile, it also takes much longer time to trigger the snapping and flipping.

Next, we further explore how the surface temperature T_{surf} affects the snapping-induced flipping behavior in the dancing ring (**Figure S7**). We find that when T_{surf} is lower than 105 °C (e.g., 90 °C), the wavy ring deforms into a trumpet shape and fails to snap, since the smaller shrinkage of LCEs cannot provide sufficient driving moment to overcome the energy barrier. When T_{surf} is over 165 °C (e.g., 180 °C), the wavy ring shows similar transient snapping and flipping behavior to the case of circular rings without waves (**Figure S4a-4b**). After 9 trials of snapping and flipping (**Figure S7**), the wavy ring shrinks to a minimum size, the same as the first-stage cured ring with R_o = 10 mm, and stops, since the temperature becomes nearly homogeneous across the height of the ring.

When T_{surf} is in the range of 105 °C to 165 °C, steady-state periodic dancing of the ring occurs through self-sustained snapping induced continuous flipping. **Figure 2f** shows the dancing frequency *f* of the flipping ring as a function of T_{surf}, where *f* is the inverse of the period *p* (i.e., $f = 1/p$), calculated by averaging the time intervals between two consecutive snapping (**Figure S7**). Interestingly, it shows a parabolic curve with its peak frequency f_{max} ~ 0.2 Hz achieved at an intermediate T_{surf} = 135 °C. As T_{surf} increases from 105 °C to 165 °C, *f* increases first from ~ 0.05 Hz to the peak of ~ 0.2 Hz at 135 °C, then decreases to the lowest frequency of ~ 0.04 Hz at 165 °C. Meanwhile, we note that the average radius *R* of the steady-state dancing ring (its original radius before heating is ~ 25 mm) decreases monotonically with the increasing T_{surf} due to its higher shrinkage of the LCEs. **Figure 2f** shows that as T_{surf} increases from 105 °C to 165 °C, *R* decreases from ~ 21 mm to ~ 15 mm, corresponding to a further ~ 29% size shrinkage.

2.2 Understanding snapping-induced dancing via simplified models and simulation

To better understand the snapping-induced flipping and dancing behavior in the ring, we combine both simplified theoretical models and finite element analysis (FEA) to evaluate the energy barrier ΔU and the driving flipping moment M_T arising from ΔT across the height.

The energy barrier ΔU can be estimated from the elastic strain energy *U* of the wavy ring with the negligible stretching energy, which can be expressed as

$$U = \int_0^l \frac{1}{2}\left(B_t \kappa_t^2 + B_b \kappa_b^2 + C\tau^2\right) ds \qquad (1)$$

where κ_t and κ_b are the two principal curvatures along the arc length of the ring and τ is the torsion of the ring (**Figure S3c**). B_t, B_b, and C denote the bending and torsional rigidities, respectively. *s* denotes the arc-length along the wavy ring and l is the perimeter of the wavy ring with the coordinates shown in **Figure S3c**. Flipping results in the variation in the binormal curvatures κ_b along the ring, where the variation in the normal curvature is neglected. Thus, the contribution to the energy variation takes the form of

$$U = 2NB_b \frac{sin^2(\theta)}{R} \tan\left(\frac{2\pi}{N}\right) \qquad (2)$$

where N is the number of semi-circles and θ is the flipping angle (**Figure S3b**). U has a peak value at $\vartheta = \pi/2$ (**Figure S3d**), which corresponds to the unstable flatten state. Thus, the energy barrier $\Delta U = U_{max} - U_{min}$ can be obtained as

$$\Delta U = \frac{2NB_b}{R} \tan\left(\frac{2\pi}{N}\right) \qquad (3)$$

Equation (3) shows that ΔU is inversely proportional to ring radius R and linearly proportional to the bending stiffness $B_b = Et^4/12$ with E being the Young's modulus.

In principle, to trigger the onset of snapping, it requires the work done by the driving moment M_T to overcome the energy barrier ΔU. Considering the discrete and heterogeneous thermal contact in the wavy ring, it is challenging to derive the explicit expression for M_T. However, an approximate scaling law can be found as[42]

$$M_T \propto B_b \alpha \Delta T \qquad (4)$$

where α is the coefficient of thermal expansion and $\Delta T \sim T_{surf} - T_{air}$ (T_{air} is the ambient temperature) is the temperature gradient across the ring height.

The simplified models provide some qualitative insights on explaining the observed peak frequency at an intermediate temperature as shown in **Figure 2f**. When T_{surf} increases, M_T will increase linearly with ΔT (Equation (4)). Thus, as expected, a higher M_T at higher T_{surf} will increase the flipping speed and thus the dancing frequency, as observed in the relatively lower surface temperature range (i.e., 105 °C ≤ T_{surf} ≤ 165 °C) in **Figure 2f**. Meanwhile, the ring radius R also decreases sharply with the increasing T_{surf} **(Figure 2f).** A reduction in R leads to an increase in the energy barrier ΔU (Equation (3)). Thus, despite the increasing M_T with T_{surf}, the driving moment is compromised by the increased energy barrier in the bistable ring, which leads to a decreasing dancing frequency with further increase of T_{surf} as observed in **Figure 2f**.

The moment-driven snapping behavior of the free-standing wavy ring on a rigid surface is further evaluated through simplified FEA simulations (**Figures 2g**-**2h**, **Movie S4**), where two ends of the wavy ring are twisted with a twisting angle of $\vartheta = 2\pi$ with the reaction moment M_R being recorded (see Materials and methods for details). **Figure 2g** shows the reaction moment-flipping angle curves of the rings with different radius. As the flipping angle ϑ increases from 0 to π (flipped), and to 2π (flip back), M_R shows a sinusoidal profile with two peaks at $\vartheta = \pi/4$ and $5\pi/4$, indicating the onsets of snap-through and snap-back process, respectively. The negative M_R indicates the bistable characteristics of the ring with zero reaction moment at $\vartheta = \pi/2$ and $3\pi/2$ representing the unstable states (**Figure 2h**, **Movie S4**). These are consistent with both experiments (**Figure 2e**) and theoretical modeling, where moment $M = \mathrm{d}U/\mathrm{d}\vartheta \propto \sin(2\vartheta)/R$ in terms of Equation (2). As the ring radius decreases, both the critical snapping moment M_{cr}, i.e., the peak moment, and the energy barrier (area underneath the M_R-ϑ curve) increase, which are consistent with both the modeling (Equations (2) and (3)) and experiments. Compared to R, the ring thickness t has a more prominent effect on ΔU and M_{cr}, where both ΔU and M_{cr} increase exponentially with t (Supporting Information, **Figure S8**). Furthermore, we note that compared to the wavy ring, its counterpart circular ring without waves shows a much higher energy barrier and a ~ 4 times higher critical snapping moment (**Figure S4c**), which makes it more challenging for the thermal actuation to overcome the energy barrier.

2.3 Twisting dancing rings for directional mobility

We note that the ring flips in place without showing directional mobility on a hot surface or under IR light. This is mainly due to the highly geometric symmetry of the circular rings (i.e., infinite lines of symmetry), which also induces nearly symmetric ring deformation and thus isotropic friction along all the directions. To achieve the directional mobility, it needs asymmetric friction.

Next, we explore both a physical and geometric way to generate asymmetric friction in the dancing rings, i.e., by means of either physically adding a lightweight roller to locally reduce friction or modifying the ring shape to break its geometric symmetry, respectively. **Figure 3a** shows that when hooping a thin lightweight aluminum foil roller around the free-standing wavy ring, it demonstrates a nearly directional crawling motion on a hot surface (T_{surf} = 150 ^{o}C) via snapping and flipping of the ring with the roller always in the rear. The roller can dramatically reduce friction in the rear to drive the forward motion.

To break the geometric symmetry in the wavy ring, we impose a symmetry line by introducing additional twisting features during fabrication to construct a twisted wavy ring. **Figure 3b** illustrates the schematics of fabricating the twisted LCE wavy ring by following the similar procedure in **Figure 1**. Differently, to generate the twisted feature, during the second-stage UV curing, a number of twists (e.g., 8 twists) are applied to the front end of the stretched wavy ring, i.e., a twist end (T-end) in **Figure 3b**, while the other end remains pinned, i.e., a pin end (P-end) in **Figure 3b**. Correspondingly, pairs of twists with opposite chirality are generated and symmetrically distributed on two sides. Thus, an axis of symmetry is pre-defined during fabrication by connecting the two twist-pin ends (i.e., the dashed T-P line in **Figure 3b**). The twisted features are preserved after UV curing and twist-pin release, as demonstrated in the fabricated twisted wavy ring in **Figure 3c**. It shows that the two sides of the ring writhe out of plane to deform into an elongated saddle-like shape.

Figure 3d, Movie S5-S6 show the representative steady-state, periodic sequential shape changes and moving gaits during its directional crawling toward the front T-end on a hot surface (T_{surf} = 150 ^{o}C). Generally, its moving direction is approximately along the pre-defined axis of symmetry (i.e., the T-P line), where the two T- and P-ends correspond to the front and rear of the crawling ring with asymmetric friction, respectively. We note that despite the shape changes in the crawling ring, its deformed shapes are almost symmetric about the T-P axis.

We note that the crawling is driven by a cyclic sequential dynamic shape-changing process, i.e., flipping-induced twist generation in the front, followed by the sequential twist propagation from the front to the end to move the ring forward. Such a dynamic process is similar to the case of manually flipping a large paper ring at the front end, as shown in **Figure 3e and Movie S7** (its inner and outer surfaces are colored in red and green, respectively, for better visualization). The front-end flipping as a twist generation source is similar to the thermal-actuated inside-out flipping of the LCE ring from the front (i.e., the T-end during fabrication). First, it generates a pair of twists with opposite chirality, followed by their sequential propagation along two sides of the perimeter from the front to rear end. Correspondingly, in the LCE ring, it propagates along the pre-defined symmetric T-P axis (**Figure 3d**). After meeting at the opposite rear end (i.e., the corresponding P-end in the LCE ring during fabrication), the pair of twists become cancelled due to their opposite chirality, which leads to snapping and writhing out of plane at the rear end. Consequently, it can largely reduce friction at the rear of the LCE ring to propel it forward. The crawling process is in analogy to a "forward driving wheel" ("FDW") locomotion mode, where the motion is driven by the rotation (i.e., inside-out flipping) of the front "wheel" (i.e., the front pre-defined twist end) to pull the soft body forward.

2.4 Tuning crawling speeds by geometric asymmetries in twisted wavy rings

Despite the promise in the achieved directional mobility in the twisted wavy ring, its crawling speed on a hot surface (T_{surf} = 150 ^{o}C) is rather slow (0.38 mm/s). To speed up its motion, we propose further enhancing the front-rear geometric asymmetry by employing a more generalized asymmetric ring model during the first-stage curing (**Figure 4a**). **Figure 4a** shows an example composed of a half circular ring and the other half wavy ring, i.e., the circumferential ratio of the wavy segment (i.e., the wave ratio) ρ_w is 50%. Similarly, the twist-pin ends (i.e., the T-P axis in **Figure 4a** with T-end and P-end in the wavy and circular end, respectively) predefines the axis of symmetry during fabrication. It, in turn, determines the approximate crawling direction, i.e., toward the T-end in the wavy ring side as discussed before. This is consistent with the observed "FWD" locomotion mode in the experiments (**Figure 4b** and **Movie S8**), which is driven by the inside-out rotation of the front wavy ring as the front "wheel".

Next, we explore the effect of the geometric asymmetry on its crawling speed by tuning ρ_w, as shown in **Figure 4c** (T_{surf} = 150 °C, the number of twists n_{twist} = 8 during the second-stage UV curing). Specially, when ρ_w = 0% or 100%, it reduces to a twisted circular ring without waves and a twisted wavy ring (i.e., the insets of **Figure 4c**), respectively, which possess the lowest level of geometrical asymmetry (LGA), while the ring with ρ_w = 50% exhibits the highest LGA. As expected, **Figure 4c** shows that the profile of the crawling speeds at different ρ_w is approximately symmetric about the axis of ρ_w = 50%. For the ring with the highest LGA of ρ_w = 50%, it shows the fastest crawling speed (~ 0.95 mm/s), whereas the rings with the lowest LGA of ρ_w = 0% or 100% show approximately the slowest speed of ~ 0.32 mm/s, which is ~ 3 times slower than the peak speed.

We further explore the effect of the number of twists n_{twist} during the second-stage UV curing on the crawling speed for the highly asymmetric rings with ρ_w = 50%. **Figure 4d** shows that as n_{twist} increases from 0 to 4, the crawling speed increases dramatically from ~ 0.21 mm/s to ~ 0.84 mm/s, which is about four fold increase. It is because the introduced twists facilitate the formation of the inside-out flipping of the front driving "wheel" to propel it forward. However, as n_{twist} further increases, the crawling speed increases slightly and approaches to a plateau, since the twists on the front "wheel" become saturated and the "wheel" transits to a helical shape. Further increase in the twist number will not dramatically change the helical shape and thus the crawling speeds barely change.

We note that the directional self-crawling in the asymmetric rings can also be achieved using the IR light. However, it crawls along an opposite direction to that on hot surfaces, i.e., toward the circular ring side without waves (**Figure 4e** and **Movie S9**). This is due to the light-induced inverted flipping, i.e., outside-in flipping. Correspondingly, the locomotion mode switches from the "FWD" on a hot surface to "rear wheel driving" ("RWD") under light, where the outside-in flipping of the wavy ring in the rear acts as both the rear "wheel" and the twist generation source, which provide the driving force to push the ring forward.

We then investigate the load carrying capacity of the ring with ρ_w = 50%. As shown in **Figure 4f** and **Movie S8**, the load or cargo is carried with the help of a sled that is driven by the crawling ring on a hot surface. The sled is made of aluminum foil and hooked to the rear side (i.e., the circular side) of the ring without interfering with the "FWD" crawling of the ring. The maximum carrying load (i.e., the wooden tablet as a cargo) is about 0.42 g, which is ~ 1.5 times heavier than the ring's self-weight (~ 0.28 g).

2.5 Aqueous self-crawling

Next, we further explore its locomotion capabilities in heated water for expanding its potential applications in autonomous aqueous crawling. Two scenarios are examined: one is in shallow water with the wavy ring (ρ_w = 50%) partially immersed in water (water depth w_d ~ 1/3 ring height); the other is in relatively deeper water with the ring fully immersed for potential underwater crawling (w_d ~ 1.5 ring height). The ring is placed in a metal pan filled with water with its bottom remaining contact with the pan. The pan is put on a hot plate (~ 260 ^{o}C) and the heated pan provides the driving force for the self-crawling ring in heated water (~ 95 ^{o}C). **Figure 5a** and **Movie S10** shows that the wavy ring can self-crawl in shallow water using a similar "FWD" mode to that on the ground.

During crawling, the front wavy side consecutively reaches out of the water surface while the rear circular side remains immersed in water. Similarly, the ring can also self-crawl underwater with the similar "FWD" mode in deep water (**Figure 5b, Movie S10**). We further compare their self-crawling speeds and find that the ring can achieve a much faster crawling speed of ~ 3.2 mm/s in shallow water, which is close to 3.4 times faster than that under water (~ 0.95 mm/s). This is due to its relatively larger thermal gradient in the heated water and cool air interface than that under water.

2.6 Self-escaping from V-shaped confined spaces

Lastly, based on the observed shape-changes during the directional crawling of the asymmetric twisted wavy ring, we further explore its potential capability of escaping from a V-shaped confined space. **Figure 6a** and **Movie S11** demonstrate that the self-crawling ring (ρ_w = 50%, n_{twist} = 8) on a hot surface (T_{surf} = 150 °C) attempts to pass through a gap with the gap size narrower than the body width of the ring. As shown in **Figure 6a(i)**, the gap confined between two heated aluminum (Al) walls is about 17 mm (~ 32%) narrower than the ring width. When the ring crawls to approach the gap in the V-shaped confined space, it is blocked by the side walls (**Figure 6a(ii)**) in the beginning. Then, after several trials of adaptive interactions between the shape-shifting body and the wall, the ring can accommodate itself by squeezing its body (**Figures 6a(iii-v)**), and successfully pass through the narrow gap (**Figure 6a(vi)**).

We also note that the ring can avoid the gap by redirecting its crawling motion when the gap size is further reduced (e.g., 19 mm (~ 36%) narrower than the ring width) (**Figure 6b** and **Movie S11**). As the ring approaches and is blocked by the walls, the ring can make turns via self-accommodations and adaptive interactions with the walls (**Figure 6b(i-v)**). Consequently, the ring can crawl back to avoid being stuck in the gap (**Figure 6b(vi)**). When the Al walls are replaced with thermal insulated paper boards, the minimum pass-through gap size increases to 40 mm (i.e., ~ 25% narrower than ring width) because of less heat absorbed from the walls (**Figure S9a**). Similarly, the ring can also crawl back when encountering an even smaller gap size (**Figure S9b**).

3. Conclusions

In this work, we design and fabricate a library of free-standing LCE wavy rings with tunable geometric asymmetries. Their geometries can be tuned to be highly symmetric or asymmetric. In turn, when placing on a hot surface or under remote IR light, these rings can self-dance in place or self-crawl in "FWD" or "RWD" modes along a pre-defined axis of symmetry during fabrication via self-sustained snapping-induced flipping. Equipped with the shape-shifting capability during crawling, the self-crawling ring can adapt its body shape to autonomously escape from confined spaces.

We envision that the strategy of combining geometric symmetry/asymmetries in the ring-like structures with the LCE materials for untethered motions could be applied to other more complex structures in different shapes and topologies, as well as other stimuli-responsive soft materials such as hydrogels, shape memory polymers and magnetic elastomers etc. This work could find potential applications in designing autonomous mobile soft robots by harnessing thermal or photothermal energy from the surrounding environments, as well as shape-adaptive soft robots.

Materials and methods

Materials: The liquid crystal mesogen 1,4-bis-[4-(3-acryloyloxypropyloxy)benzoyloxy]-2-methylbenzene (RM 257), was purchased from Wilshire Technologies (Princeton, NJ, USA). The chain extender 2,2'-(ethylenedioxy) diethanethiol (EDDET), crosslinker pentaerythritol tetrakis (3-mercaptopropionate) (PETMP), photoinitiator (2-hydroxyethoxy)-2-methylpropiophenone (HHMP), and catalyst dipropyl amine (DPA) were purchased from Sigma Aldrich. All the chemicals were utilized without further modification.

Silicone rubber mold fabrication: Master molds with different sample shapes of wavy rings and wavy-circular rings were 3D printed with a commercialized 3D printer (Objet 260, Connex 3, Stratasys), followed by cleaning in ultrasonication bath to remove the chemical residues. Then silicone rubber (Ecoflex 00-50, Smooth-On Inc.) was carefully poured in the 3D printed masters, and degassed for 5 min. After cured in an oven at 70 ^{o}C for 30 min, the silicone molds were removed from the masters.

LCE sample fabrication: The LCE samples were synthesized by modifying previously reported thiol-acrylate Michael addition reaction method [40-41]. In a typical synthesis process, 2 g of RM 257 was fully dissolved in 0.7 g of toluene at 85 ^{o}C, and cooled down to room temperature. Next, 0.18 g of PETMP, 0.42 g of EDDET, and 0.012 g of HHMP were added into the solution. After mixed at 85 ^{o}C, the solution was cooled down to room temperature again, and 0.29 g of DPA solution (2 wt%, in toluene) was added. After fully mixed and degassed, the solution was poured in the silicone rubber mold, and placed in a closed container overnight for fully reaction. A first stage LCE sample can be obtained after dried in oven at 80 ^{o}C for one day. Finally, the LCE samples were radially stretched to hoop on a 3D printed cylinder and exposed to 365 nm UV irradiation for 10 min under different stretching and twisting strategies.

Characterization methods: The infrared videos and images were taken with an infrared camera (FLIR A655sc). The high-speed videos were taken with a high-speed camera (Fastcam SA-X2, Photron).

Finite element analysis (FEA) simulation: FEA simulation was performed with commercial software Abaqus/Explicit to simulate the snapping behavior of the wavy rings during flipping. The LCE is modeled as linear elastic materials with Young's modulus 11MPa and Poisson's ratio 0.3. Wavy rings with different radii (i.e., 21 mm, 18 mm, and 15 mm) were simulated while thickness t = 1 mm and ring height h = 5 mm are kept the same. A pair of flipping loads with opposite directions were applied to the two ends of the wavy rings by means of twist angle loading and the rings were free to rotate along the circumference. The twist angle, i.e., the flipping angle, increases from 0 to 2π to simulate two trails of flipping with the reaction moments being recorded during the flipping.

Supporting Information

Supporting Information is available from the Wiley Online Library or from the corresponding authors.

Acknowledgments

J. Y. acknowledges the funding support from NSF (CMMI-2005374 and CMMI- 2126072). H. S. acknowledges the funding support from NSF 2026622.

Competing Interests

The authors declare no competing interests.

Data Availability Statement

All study data are included in the article and/or supporting information.

Author Contribution

Y.Z. and J.Y. developed the concept and designed the experiments. Y.Z. and F.Q. fabricated and characterized the prototypes. Y.H. conducted the theoretical modeling. Y.C. conducted the finite element simulation. Y.Z., and Y.H., drafted the manuscript. J.Y. and H.S. revised the manuscript. All the authors contributed to the discussion, data analysis, and edit of the manuscript.

References

1. Chi, Y.; Li, Y.; Zhao, Y.; Hong, Y.; Tang, Y.; Yin, J., Bistable and Multistable Actuators for Soft Robots: Structures, Materials, and Functionalities. *Advanced Materials* **2022,** *34* (19), 2110384.
2. Hu, N.; Burgueño, R., Buckling-induced smart applications: recent advances and trends. *Smart Materials and Structures* **2015,** *24* (6), 063001.
3. Bertoldi, K., Harnessing instabilities to design tunable architected cellular materials. *Annual Review of Materials Research* **2017,** *47*, 51-61.
4. Zhao, Q.; Yang, X.; Ma, C.; Chen, D.; Bai, H.; Li, T.; Yang, W.; Xie, T., A bioinspired reversible snapping hydrogel assembly. *Materials Horizons* **2016,** *3* (5), 422-428.
5. Fan, W.; Shan, C.; Guo, H.; Sang, J.; Wang, R.; Zheng, R.; Sui, K.; Nie, Z., Dual-gradient enabled ultrafast biomimetic snapping of hydrogel materials. *Science Advances* **2019,** *5* (4), eaav7174.

6. Shankar, M. R.; Smith, M. L.; Tondiglia, V. P.; Lee, K. M.; McConney, M. E.; Wang, D. H.; Tan, L.-S.; White, T. J., Contactless, photoinitiated snap-through in azobenzene-functionalized polymers. *Proceedings of the National Academy of Sciences* **2013,** *110* (47), 18792-18797.
7. Wu, S.; Baker, G. L.; Yin, J.; Zhu, Y., Fast Thermal Actuators for Soft Robotics. *Soft Robotics* **2021**.
8. Ramachandran, V.; Bartlett, M. D.; Wissman, J.; Majidi, C., Elastic instabilities of a ferroelastomer beam for soft reconfigurable electronics. *Extreme Mechanics Letters* **2016,** *9*, 282-290.
9. Liu, J. A. C.; Gillen, J. H.; Mishra, S. R.; Evans, B. A.; Tracy, J. B., Photothermally and magnetically controlled reconfiguration of polymer composites for soft robotics. *Science Advances* **2019,** *5* (8), eaaw2897.
10. Jiang, Y.; Korpas, L. M.; Raney, J. R., Bifurcation-based embodied logic and autonomous actuation. *Nature Communications* **2019,** *10* (1), 128.
11. Koh, J.-S.; Yang, E.; Jung, G.-P.; Jung, S.-P.; Son Jae, H.; Lee, S.-I.; Jablonski Piotr, G.; Wood Robert, J.; Kim, H.-Y.; Cho, K.-J., Jumping on water: Surface tension–dominated jumping of water striders and robotic insects. *Science* **2015,** *349* (6247), 517-521.
12. Baumgartner, R.; Kogler, A.; Stadlbauer, J. M.; Foo, C. C.; Kaltseis, R.; Baumgartner, M.; Mao, G.; Keplinger, C.; Koh, S. J. A.; Arnold, N.; Suo, Z.; Kaltenbrunner, M.; Bauer, S., A Lesson from Plants: High-Speed Soft Robotic Actuators. *Advanced Science* **2020,** *7* (5), 1903391.
13. Pal, A.; Restrepo, V.; Goswami, D.; Martinez, R. V., Exploiting Mechanical Instabilities in Soft Robotics: Control, Sensing, and Actuation. *Advanced Materials* **2021,** *33* (19), 2006939.
14. Cao, Y.; Derakhshani, M.; Fang, Y.; Huang, G.; Cao, C., Bistable Structures for Advanced Functional Systems. *Advanced Functional Materials* **2021,** *31* (45), 2106231.
15. Overvelde, J. T. B.; Kloek, T.; D'haen, J. J. A.; Bertoldi, K., Amplifying the response of soft actuators by harnessing snap-through instabilities. *The Proceedings of the National Academy of Sciences of the United States of America* **2015,** *112*, 10863-10868.
16. Tang, Y.; Chi, Y.; Sun, J.; Huang, T.-H.; Maghsoudi, O. H.; Spence, A.; Zhao, J.; Su, H.; Yin, J., Leveraging elastic instabilities for amplified performance: Spine-inspired high-speed and high-force soft robots. *Science Advances* **2020,** *6* (19), eaaz6912.
17. Chi, Y.; Tang, Y.; Liu, H.; Yin, J., Leveraging Monostable and Bistable Pre-Curved Bilayer Actuators for High-Performance Multitask Soft Robots. *Advanced Materials Technologies* **2020,** *5* (9), 2000370.
18. Lee, H.; Xia, C.; Fang, N. X., First jump of microgel; actuation speed enhancement by elastic instability. *Soft Matter* **2010,** *6* (18), 4342-4345.
19. Koh, J.-S.; Yang, E.; Jung, G.-P.; Jung, S.-P.; Son, J. H.; Lee, S.-I.; Jablonski, P. G.; Wood, R. J.; Kim, H.-Y.; Cho, K.-J., Jumping on water: Surface tension–dominated jumping of water striders and robotic insects. *Science* **2015,** *349* (6247), 517-521.
20. Gorissen, B.; Melancon, D.; Vasios, N.; Torbati, M.; Bertoldi, K., Inflatable soft jumper inspired by shell snapping. *Science Robotics* **2020,** *5* (42), eabb1967.
21. Kim, Y.; van den Berg, J.; Crosby, A. J., Autonomous snapping and jumping polymer gels. *Nature Materials* **2021,** *20* (12), 1695-1701.
22. Zhao, Y.; Chi, Y.; Hong, Y.; Li, Y.; Yang, S.; Yin, J., Twisting for soft intelligent autonomous robot in unstructured environments. *Proceedings of the National Academy of Sciences* **2022,** *119* (22), e2200265119.
23. Yasuda, H.; Buskohl, P. R.; Gillman, A.; Murphey, T. D.; Stepney, S.; Vaia, R. A.; Raney, J. R., Mechanical computing. *Nature* **2021,** *598* (7879), 39-48.
24. Wie, J. J.; Shankar, M. R.; White, T. J., Photomotility of polymers. *Nature Communications* **2016,** *7* (1), 13260.
25. Pang, X.; Lv, J.-a.; Zhu, C.; Qin, L.; Yu, Y., Photodeformable Azobenzene-Containing Liquid Crystal Polymers and Soft Actuators. *Advanced Materials* **2019,** *31* (52), 1904224.

26. Xiao, Y.-Y.; Jiang, Z.-C.; Zhao, Y., Liquid Crystal Polymer-Based Soft Robots. *Advanced Intelligent Systems* **2020,** *2* (12), 2000148.
27. Zhao, T.; Fan, Y.; Lv, J.-a., Photomorphogenesis of Diverse Autonomous Traveling Waves in a Monolithic Soft Artificial Muscle. *ACS Applied Materials & Interfaces* **2022,** *14* (20), 23839-23849.
28. Kim, J. G.; Jeon, J.; Sivakumar, R.; Lee, J.; Kim, Y. H.; Cho, M.; Youk, J. H.; Wie, J. J., Light-Fueled Climbing of Monolithic Torsional Soft Robots via Molecular Engineering. *Advanced Intelligent Systems* **2022,** *4* (3), 2100148.
29. Zhao, T.; Fang, W.; Fan, Y.; Hu, Z.; Wu, H.; Feng, X.-Q.; Lv, J.-a., Phototactic Miniature Soft Robots with Terrain Adaptability. *Advanced Materials Technologies* **2022,** *7* (9), 2101660.
30. Ahn, C.; Li, K.; Cai, S., Light or Thermally Powered Autonomous Rolling of an Elastomer Rod. *ACS Applied Materials & Interfaces* **2018,** *10* (30), 25689-25696.
31. Xia, Y.; Cedillo-Servin, G.; Kamien, R. D.; Yang, S., Guided Folding of Nematic Liquid Crystal Elastomer Sheets into 3D via Patterned 1D Microchannels. *Advanced Materials* **2016,** *28* (43), 9637-9643.
32. Kamal, T.; Park, S.-Y., A liquid crystal polymer based single layer chemo-responsive actuator. *Chemical Communications* **2014,** *50* (16), 2030-2033.
33. Korner, K.; Kuenstler, A. S.; Hayward, R. C.; Audoly, B.; Bhattacharya, K., A nonlinear beam model of photomotile structures. *Proceedings of the National Academy of Sciences* **2020,** *117* (18), 9762.
34. Gelebart, A. H.; Jan Mulder, D.; Varga, M.; Konya, A.; Vantomme, G.; Meijer, E. W.; Selinger, R. L. B.; Broer, D. J., Making waves in a photoactive polymer film. *Nature* **2017,** *546* (7660), 632-636.
35. Shahsavan, H.; Aghakhani, A.; Zeng, H.; Guo, Y.; Davidson, Z. S.; Priimagi, A.; Sitti, M., Bioinspired underwater locomotion of light-driven liquid crystal gels. *Proceedings of the National Academy of Sciences* **2020,** *117* (10), 5125-5133.
36. Jeon, J.; Choi, J.-C.; Lee, H.; Cho, W.; Lee, K.; Kim, J. G.; Lee, J.-W.; Joo, K.-I.; Cho, M.; Kim, H.-R.; Wie, J. J., Continuous and programmable photomechanical jumping of polymer monoliths. *Materials Today* **2021,** *49*, 97-106.
37. Clement, A.; Babaei, M.; Phadikar, J.; Lee, D. W.; Skandani, A. A.; Shankar, M. R., Complexity from simplicity: Confinement directs morphogenesis and motility in nematic polymers. *Extreme Mechanics Letters* **2021,** *47*, 101362.
38. Yoshiaki, G.; Yasuhito, W.; Toshihiro, K.; Makoto, O., Elastic buckling phenomenon applicable to deployable rings. *International Journal of Solids and Structures* **1992,** *29* (7), 893-909.
39. Goriely, A., Twisted Elastic Rings and the Rediscoveries of Michell's Instability. *Journal of Elasticity* **2006,** *84* (3), 281-299.
40. Yakacki, C. M.; Saed, M.; Nair, D. P.; Gong, T.; Reed, S. M.; Bowman, C. N., Tailorable and programmable liquid-crystalline elastomers using a two-stage thiol–acrylate reaction. *RSC Advances* **2015,** *5* (25), 18997-19001.
41. Barnes, M.; Verduzco, R., Direct shape programming of liquid crystal elastomers. *Soft Matter* **2019,** *15* (5), 870-879.
42. Baumann, A.; Sánchez-Ferrer, A.; Jacomine, L.; Martinoty, P.; Le Houerou, V.; Ziebert, F.; Kulić, I. M., Motorizing fibres with geometric zero-energy modes. *Nature Materials* **2018,** *17* (6), 523-527.

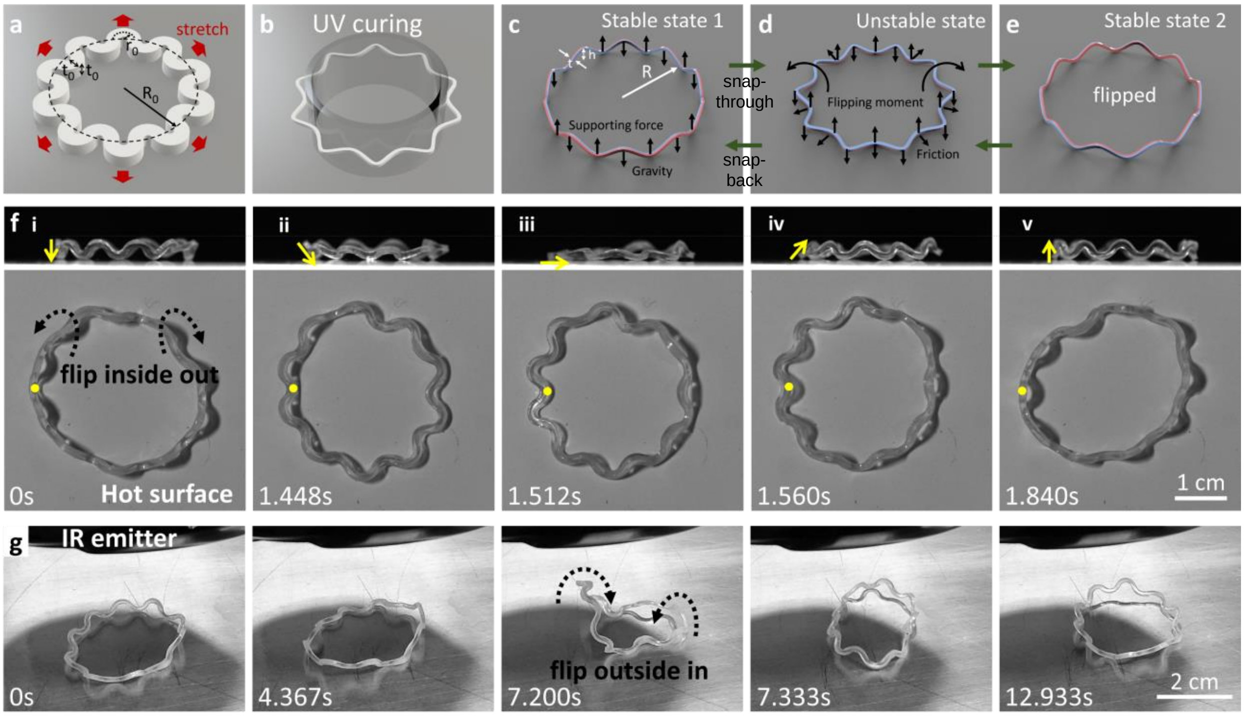

Figure 1. Snapping-induced self-flipping dancing motion in a freestanding LCE wavy ring under thermal and photothermal actuation. (a-b) Schematics of fabricating the wavy ring by following the two-stage curing. The first-stage ring is radially stretched (a, R_o = 10 mm, r_o = 1.6 mm, and t_o = 2 mm) and hooped onto a cylinder for the second-stage UV curing (b). (c-e) Schematics of the thermal-actuated bistable flipping switch in the fabricated freestanding wavy ring by bypassing the unstable flatten state (d). The shrinkage in the wave troughs leads to its transition to a trumpet-like shape to break the originally balanced supporting fore and gravity. It creates the moment to drive the flipping (d). (f) The time-lapsed optical side-view and top-view images of the self-dancing ring (R ~ 25 mm, h ~ 5 mm, and t ~ 1 mm) on a hot plate with surface temperature of 120 ^{o}C. The snap through happens within 112 milliseconds from (ii) to (iv). The yellow arrows indicate the snapping-induced inside-out flipping. (g) The time-lapsed optical images of the self-dancing ring under a 250 W IR emitter. The distance between the IR emitter and sample is ~ 8 cm. It snaps to flip outside in with more complex out-of-plane bending deformation within 133 milliseconds from (iii) to (iv).

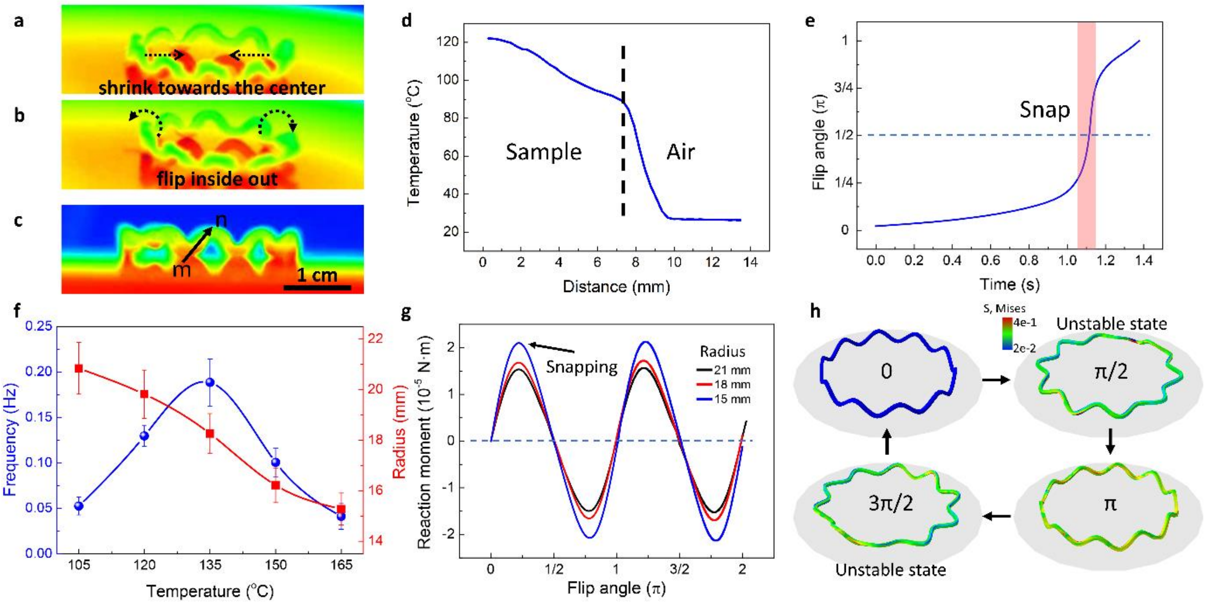

Figure 2. Snapping-induced self-dancing ring performances and mechanisms. (a-c) The infrared images of the dancing ring on a hot surface (120 ^{o}C) in different representative deformed states. The wave troughs of the ring shrink toward the center (a) and transit to a trumpet-like shape and flip inside out (b). It shows a thermal gradient (c) with the temperature profile along the path mn shown in (d). (e) The changes of the measured flipping angle with the time during one cycle of inside-out flipping. The shaded area with a dramatic change in the flipping angle indicates the snap-through process. (f) The steady-state self-dancing frequencies (blue curve) and radius change (red curve) of the ring as a function of the hot surface temperatures. (g) The FEA simulated reaction moment-flip angle curves for the rings with different radius during one cycle of snap-through and snap-back process. (h) The simulated representative shape changes in the ring at different flipping angles.

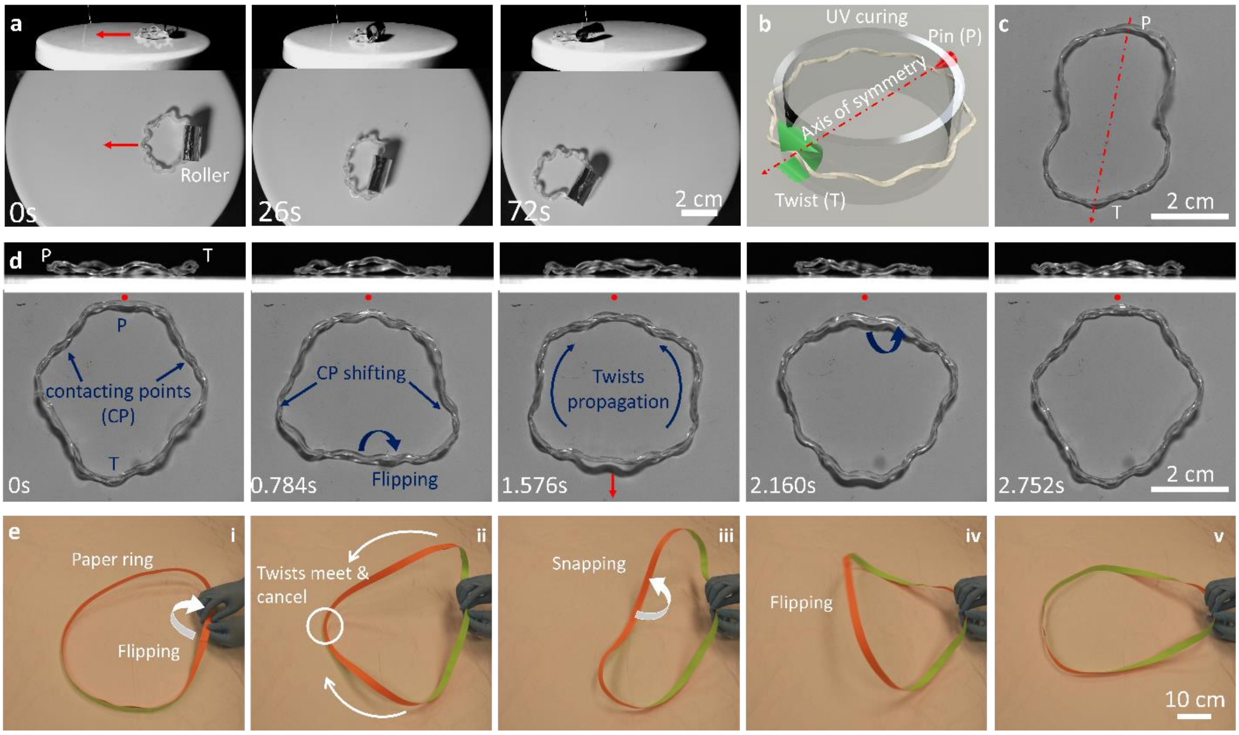

Figure 3. Directional mobility of the dancing rings with reduced symmetries to generate asymmetric front-rear friction on a hot surface (~ 150 °C). (a) The originally immobile dancing wavy ring self-crawls forward after adding a lightweight roller (aluminum tube) to reduce friction in the rear. (b) Schematics of fabricating a modified twisted wavy ring by introducing twists at one end with the other end pinned during the second-stage UV curing. The two twist-pin (T-P) ends define an axis of symmetry to largely reduce the highly geometric symmetries in the original wavy rings without twists, and the moving direction. (c) The fabricated free-standing twisted wavy ring. (d) The time-lapsed side-view and top-view images of the crawling twisted wavy ring. It moves toward the T-end along the T-P axis of symmetry. (e) Illustration of the crawling mechanism in (d) by manually twisting a paper ring from one end. The crawling in (d) is driven by twist generation (i) at one end (T-end in (d)), and twist propagation and cancelation (ii) at the other end (P-end in (d)), which induces snapping and flipping (iii-iv) to reduce its friction.

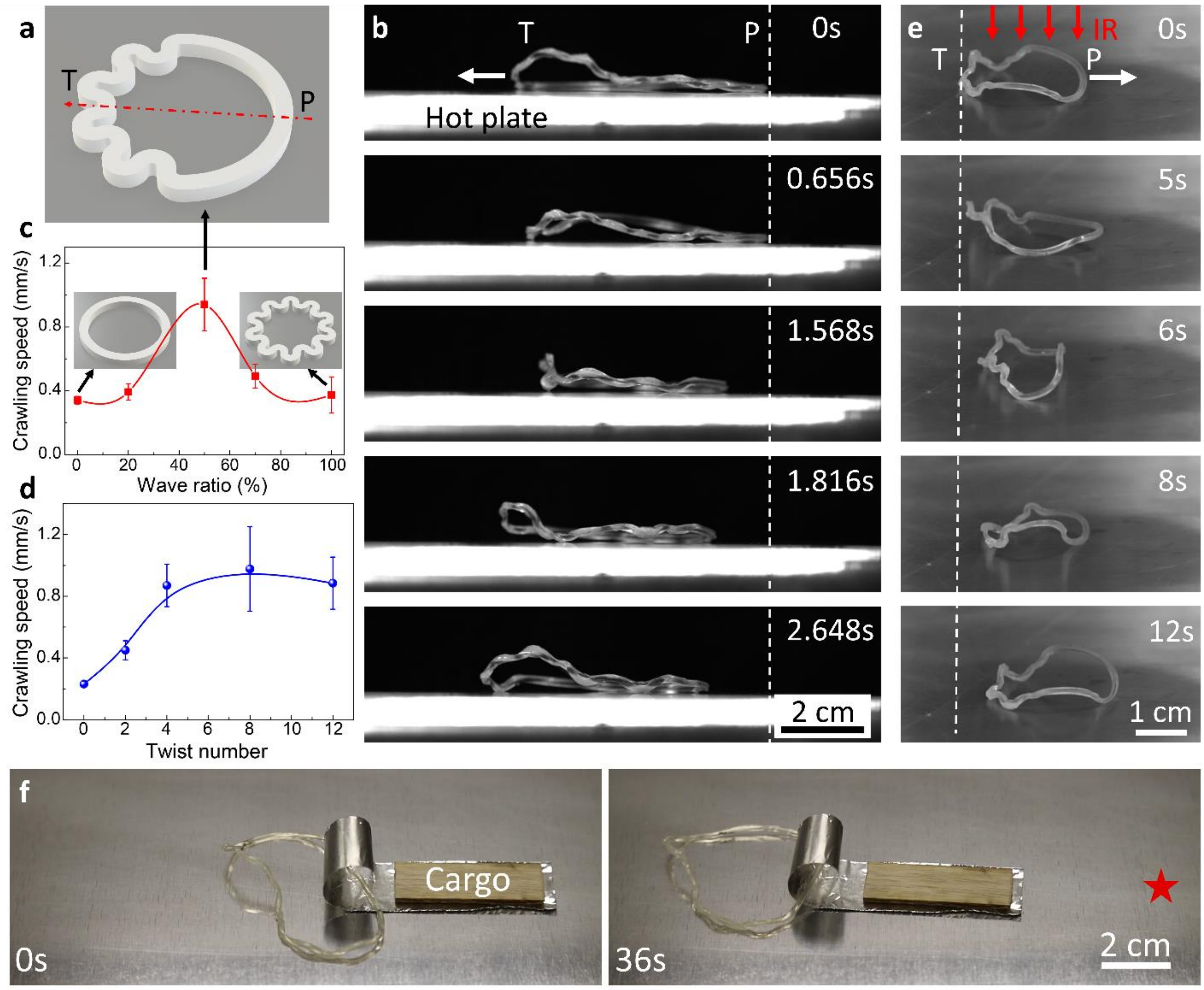

Figure 4. Self-crawling asymmetric twisted wavy rings with tunable moving speeds by geometric asymmetries. (a) Schematics of designing a modified generalized ring with geometric asymmetries by tuning the segment ratio between the wavy and circular part during the first-stage curing. It shows a special case with a half wavy segment and the other half circular segment without waves (i.e., wave ratio ρ_w = 50%). The T-P axis (dashed line) defines the twist-pin ends during the second-stage curing. (b) The time-lapsed side-view images of the crawling asymmetric twisted wavy ring with ρ_w = 50% on a hot surface (~ 150 °C) that moves toward the T-end. (c) The effect of the wave ratio ρ_w on the crawling speeds on a hot surface (~ 150 °C). Insets show the schematics of two special cases (the designs in the first-stage curing) with ρ_w = 0% (a twisted circular ring without waves) and 100% (a twisted wavy ring in Figure 3b). The twist number n_{twist} applied during the second-stage curing is 8. (d) The effect of twist number n_{twist} on the crawling speeds of the rings with ρ_w = 50% on a hot surface (~ 150 °C). (e) The time-lapsed images of the crawling ring with ρ_w = 50% under a 250 W IR emitter that moves toward the opposite P-end. The distance between the IR emitter and the

sample is ~ 8 cm. (f) The ring with ρ_w = 50% crawling on a hot surface (~ 150 ^{o}C) with a carried load (0.42g) that is about 1.5 times the ring's self-weight. The star denotes the initial position.

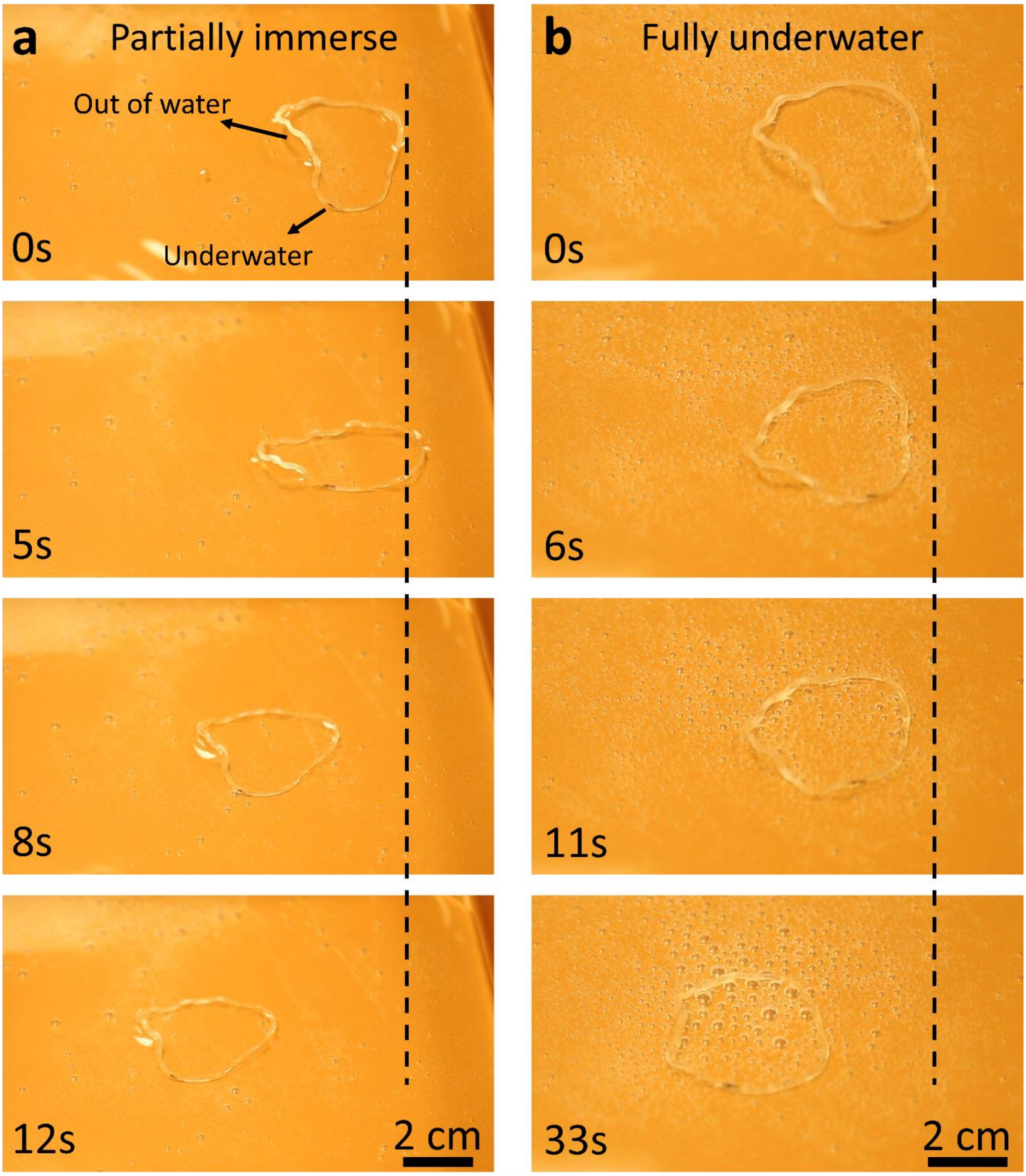

Figure 5. Self-crawling in hot water. The time-lapsed top-view images of the crawling twisted wavy ring with ρ_w = 50% when partially immersed (a) and fully immersed (b) in hot water (~ 95 °C). The water is heated in a metal pan that is placed on a 260 °C hot plate.

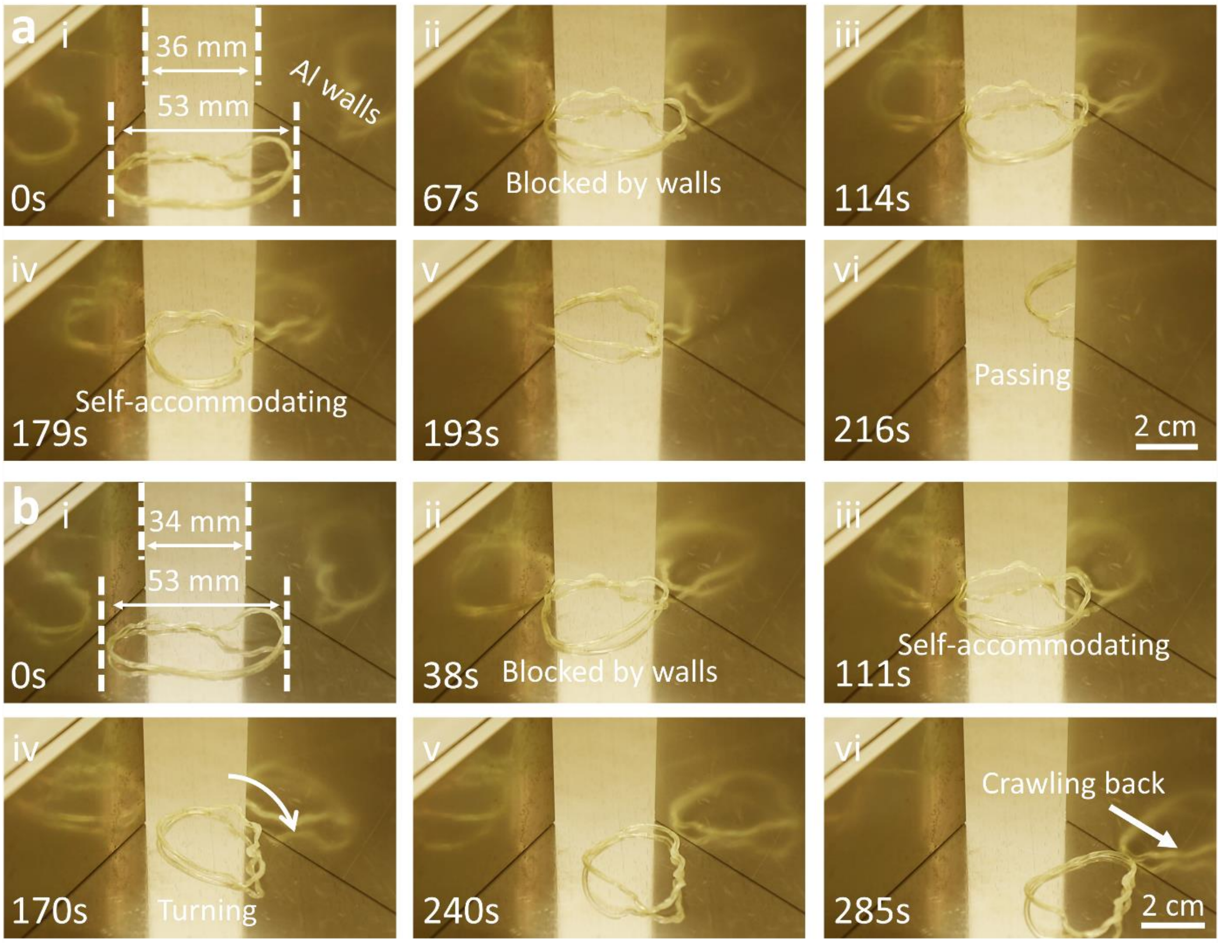

Figure 6. Self-navigating through or avoiding a confined V-shaped space of the asymmetric twisted wavy ring with ρ_w = 50% on a hot surface (~ 150 ^{o}C). (a) The processes of the ring passing through a narrow gap confined with heated aluminum walls via adaptive shape changes and interactions with the side walls. The gap is about 17 mm (~ 32%) narrower than that of the ring width. (b) The process of the ring avoiding the narrower gap by making turns and crawling back. The gap is about 19 mm narrower than that of the ring width.

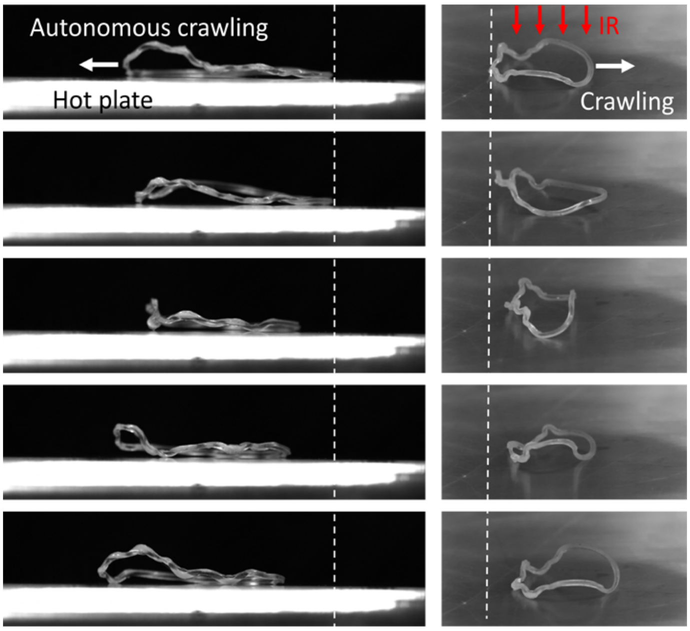

Achieving self-sustained snapping and motion remains challenging in autonomous systems. We report harnessing wavy ribbon rings for realizing self-sustained snapping in liquid crystal elastomer rings under constant temperature and light. It drives continuous flipping for either periodic self-dancing in place in symmetric rings or self-crawling in asymmetric rings on the ground and underwater, as well as self-escaping from confined spaces.